SAND2018-9525J

**Noname manuscript No.**
(will be inserted by the editor)

# Computational Study of Fermi Kinetics Transport Applied to Large-Signal RF Device Simulations

**Nicholas C. Miller · Matt Grupen · Kris Beckwith · David Smithe · John D. Albrecht**

Received: date / Accepted: date

**Abstract** A detailed description and analysis of the Fermi kinetics transport (FKT) equations for simulating charge transport in semiconductor devices is presented. The fully coupled nonlinear discrete FKT equations are elaborated, as well as solution methods and work-flow for the simulation of RF electronic devices under large-signal conditions. The importance of full wave electromagnetics is discussed in the context of high speed device simulation and the meshing requirements to integrate the full wave solver with the transport equations are given in detail. The method includes full semiconductor band structure effects to capture the scattering details for the Boltzmann transport equation (BTE). The method is applied to high speed gallium nitride (GaN) devices. Finally, numerical convergence and stability examples provide insight into the mesh convergence behavior of the deterministic solver.

N. C. Miller* · J. D. Albrecht
Department of Electrical and Computer Engineering
Michigan State University
428 S. Shaw Lane, East Lansing, MI 48824
E-mail: mill1825@egr.msu.edu

M. Grupen
Air Force Research Laboratory, Sensors Directorate
2241 Avionics Circle, WPAFB, OH, 45433, USA

K. Beckwith
Sandia National Laboratories
Albuquerque, NM 87185-1189, USA

D. Smithe
Tech-X Corporation
5621 Arapahoe Avenue Suite A, Boulder, CO 80303, USA

* N. C. Miller is now at Air Force Research Laboratory, Sensors Directorate.

**Keywords** FKT · Deterministic Boltzmann solver · Electronic device simulations · GaN high electron mobility transistor technology

## 1 Introduction

Physics based modeling of GaN high electron mobility transistor (HEMT) power amplifiers (PAs) offers a promising alternative to high frequency and large signal measurements. The physics based technology computer aided design (TCAD) tool, however, must accurately capture the physical processes in the device to provide useful data to radio frequency (RF) circuit designers. The salient features required in the TCAD tool for accurate large signal RF simulations include electronic band structure, hot electron effects, self heating, scattering, trapping, and full wave electromagnetics (EM).

Charge transport in semiconductors can be determined by the solution of the semi-classical BTE [1]

$$\frac{\partial f(\mathbf{k},\mathbf{r},t)}{\partial t} + \mathbf{v}\cdot\nabla_r f(\mathbf{k},\mathbf{r},t) + \frac{\mathbf{F}}{\hbar}\cdot\nabla_k f(\mathbf{k},\mathbf{r},t) = \left(\frac{\partial f(\mathbf{k},\mathbf{r},t)}{\partial t}\right)_{coll}. \quad (1)$$

Here, $f$ is the distribution function, $\mathbf{F}$ represents external forces acting on the distribution of particles, $\hbar$ is Planck's constant, $\mathbf{v}$ is the group velocity of the particles, and $\mathbf{k}$, $\mathbf{r}$ and t represent reciprocal space, real space and time, respectively.

The BTE is an integro-differential equation and describes how a collection of particles responds to EM fields and scattering potentials. The distribution function $f(\mathbf{k},\mathbf{r},t)$ gives the occupation probability at $\mathbf{r}$ and $\mathbf{k}$ at time $t$. It can be found by solving Eqn. (1), but

approximations are required in order to yield tractable solutions for realistic applications.

A powerful statistical method for solving the BTE is the Monte Carlo technique [2]. Monte Carlo was first presented as a statistical approach to solving general integro-differential equations [3]. Since then, it has seen a wide variety of applications, and is one of the preferred methods for accurate numerical simulation of semiconductor devices. Many flavors exist in the literature including the ensemble Monte Carlo (EMC) method [4]. It is well known, however, that the EMC method comes at an immense computational cost. The cellular Monte Carlo (CMC) algorithm was developed to reduce the burdensome high computational demands [5]. Even after sophisticated algorithms such as scattering rate precomputation and tabulation, CMC is still computationally intensive and can lead to long simulation times for complex devices. Coupling full-wave EM to EMC has also proved to be challenging and computationally expensive [6,12,13].

Despite the computational burden, many EMC and CMC methods have successfully simulated GaN HEMT technology. Variations include quantum corrected full-band CMC simulations [7] and electro-thermal MC models with self-heating effects [8,10,11]. Further EMC simulations have investigated large signal RF performance [12,13] and the effects of source-gate spacing [9].

An alternative approach to solving the BTE is accomplished through deterministic methods. These rely on taking moments of the BTE. One of the first deterministic Boltzmann solvers for semiconductor device simulations was presented in the paper by Scharfetter and Gummel [14]. This work presented physical approximations to the phenomenological drift-diffusion (D-D) model of charge transport. The physical size of the device technology was still relatively large and the numerical solution of the D-D model produced satisfactory results. However, reduced device features produce larger electric fields and hot electron effects, such as electron velocity saturation, rendering the D-D approximation insufficiently accurate.

Two seminal works which extended the D-D model to include carrier heating were presented by Stratton [15] and Blotekjaer [16]. These methods utilized different approximations of the BTE. Stratton proposed that the distribution function be split into even and odd components while Blotekjaer derived moments of the BTE without any assumptions on the form of the distribution function. Both methods required closure relations to generate a linearly independent system of equations [17] as well as further approximations to yield tractable solutions. A common closure relation is the prescription of electronic heat flow with Fourier's law [17]. One approximation used to specify momentum and energy in hydrodynamic models is parabolic band structure [17]. However, this approximation will reduce the accuracy of the device solver when the electric field is large. To the best of the authors' knowledge, no hydrodynamic or energy-transport model can include complete electronic band structure effects without the use of phenomenological models. Thus, some device solvers employ fitting parameters such as field- and temperature-dependent mobilities to improve upon the parabolic band approximation [18].

Hydrodynamic solvers are widely used in the device simulation community for analysis and characterization of power transistors. An AlGaN/GaN HEMT with surface traps was investigated with the commercially available DESSIS hydrodynamic software in [19]. This contribution did not include RF simulations, however. Self heating and hot electron effects were studied in AlGaN/GaN double-channel HEMTs in [20], but also did not include RF simulations. Finally, the 2D device simulator Minimos-NT [21] was used to accurately simulate both the static and small-signal response of several GaN HEMTs. A field-dependent mobility was tuned in [21] to accurately model the velocity saturation in GaN. Hydrodynamic solvers rarely incorporate full wave EM, with the exception of a 2D solver used to simulate terahertz plasma waves [22].

FKT is a deterministic Boltzmann solver which has shown promising results. Historically, FKT was conceived by seeking an alternative method for calculating the electronic heat flow. Rather than use the combination of Fourier's law and an approximate thermal conductivity [17], it was proposed that a thermodynamic identity could be used as a closure relation for energy-transport models [23]. This closure relation provided a robust Boltzmann solver, and it was later shown that FKT could incorporate electronic band structure [24] and full wave EM [25]. In particular, a version of FKT with GaAs band structure, quantum scattering, and hot electron effects was shown to reproduce the electron velocity overshoot and saturation calculated by sophisticated MC methods [24] in a fraction of the computational time. FKT was also shown to accurately simulate a GaAs metal semiconductor field effect transistor (MESFET) and a GaN HEMT from DC up through mm-wave frequencies without adjustable calibration parameters [24,26].

This paper presents a detailed description and analysis of the discrete nonlinear system of equations used to simulate charge transport coupled to full wave EM in the FKT device solver. The computational aspects of the discrete form of the equations have not been elaborated previously and are critical for wider use of the

methodology. First, a detailed discussion of the device simulation framework's meshing requirements is presented in Section 2. Next, the system of discrete nonlinear equations are reported in Section 3 followed by a discussion of solution variable assignment in real and energy space, a discussion of the numerical solution of the nonlinear equations, and numerical details of the different device solve types. Detailed descriptions of the boundary conditions (BCs) required for high speed device simulations are presented in Section 4. Finally, the mesh convergence and stability of the FKT device simulation framework are investigated in Sections 5 and 6, respectively.

## 2 The Delaunay-Voronoi Mesh

An important discretization technique used in the semiconductor device simulation community is the box integration method [27]. To properly discretize the divergence of a vector field with the box integration method, a special type of mesh called a Delaunay mesh [28] is required. A 2D Delaunay mesh is a set of polygons where the circumcircle of any polygon contains no points of the mesh. The points of each polygon lie on the perimeter of its respective circumcircle. The 3D analogue is a set of polyhedra with circumspheres. An example of a Delaunay triangulation of a random set of points is shown in Figure 1. The Bowyer-Watson algorithm, detailed in [29,30], was used to generate this triangulation. In the left of Figure 1, the Delaunay triangles are drawn in black and the Voronoi cells (most commonly referred to as the Voronoi diagram [31]) corresponding to the interior Delaunay nodes are drawn in red. Two circumcircles which inscribe triangles are also drawn in gray. This simple triangulation demonstrates the powerful relationship between the Delaunay triangles and the Voronoi polygons. Each Voronoi polygon corresponds to a single Delaunay node in the mesh. The faces of this Voronoi polygon (edges) correspond to edges which are connected to the Voronoi polygon's node. The normals of the Voronoi polygon's faces point in the *exact* same direction as their corresponding Delaunay edges, by construction. The importance of this relationship now becomes clear in terms of the box integration method. A divergence of a vector field integrated over each Voronoi polygon can be represented as a discrete summation of fluxes, defined on the Delaunay edges, across each face of the Voronoi polygon. This is the crux of the box integration method [27]. One divergence stencil corresponding to the shaded Voronoi polygon is illustrated in Figure 1 (right).

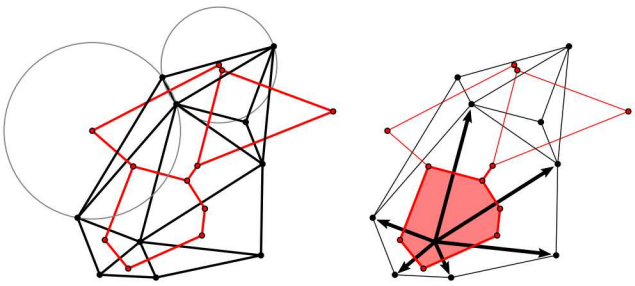

**Fig. 1** (left) The Delaunay triangulation of a random set of ten points. The Bowyer-Watson algorithm was used to create this triangulation. The Delaunay triangles are illustrated in black and the Voronoi cells in red. Only the Voronoi cells corresponding to interior Delaunay points are shown. Two circumcircles of the Delaunay triangles are also included. (right) One of the divergence stencils corresponding to the shaded Voronoi cell is outlined with arrows.

The collection of the Delaunay elements and the Voronoi diagram will here on out be referred to as the Delaunay-Voronoi (DV) mesh. Furthermore, the nodes and edges of the Delaunay elements are called primary nodes and primary edges, respectively. Dual nodes and dual edges refer to those comprising the Voronoi diagram.

There exists a wide range of algorithms to generate Delaunay triangulations. Included is the Bowyer-Watson algorithm, as well as other standard methods used in computational geometry [32,33]. These methods are reliably used to generate meshes for the finite element method (FEM), among many other computational techniques. Any arbitrary Delaunay meshing algorithm alone, however, does not produce adequate meshes for simulating semiconductor devices with the box integration method.

To elaborate on the difficulties of generating a quality DV mesh for discretization with the box integration method, a simple MESFET geometry is considered. The device consists of a thin semiconductor on top of a larger substrate. These types of features are common in electronic devices. Figure 2 illustrates an attempt at meshing a basic MESFET with an open-source Delaunay meshing tool. The code is Gmsh [34], which uses the software TetGen [35] as its Delaunay mesher. It is evident that Voronoi polygons corresponding to certain interior mesh points, each lying within one particular material, cross material interfaces as well as the boundaries of the problem domain. This is due to obtuse angles in triangles whose circumcenters fall outside of the domain boundary. A characteristic like this will not allow proper simulation of electronic devices as the charge densities must be uniquely defined in each material. Furthermore, numerical BCs rely on proper truncation of the Voronoi cells at mesh boundaries.

As an attempt to fix the Voronoi polygons, the mesh is refined in the semiconductor region. Figure 3 illus-

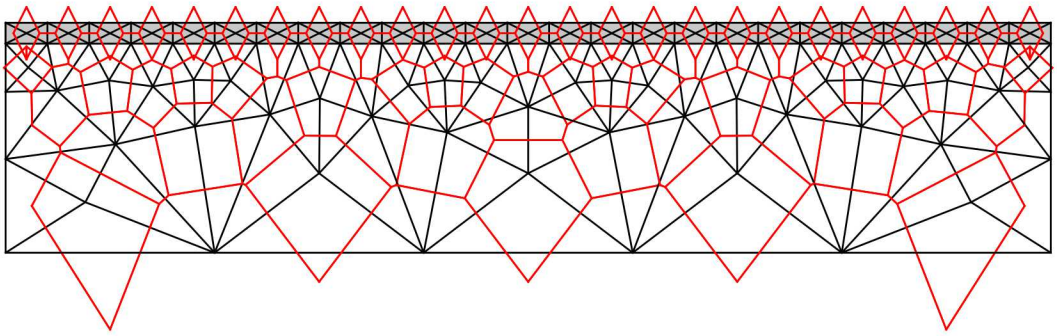

**Fig. 2** The Delaunay triangulation (black lines) and the corresponding Voronoi diagram (red lines) of the basic outline of a MESFET. This mesh was generated with the open source program Gmsh which uses the TetGen Delaunay triangulator.

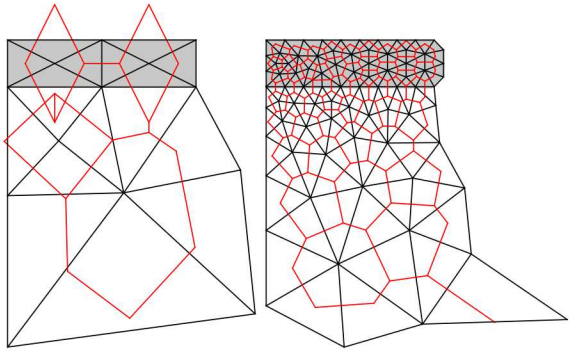


**Fig. 3** A zoom of the Gmsh generated Delaunay mesh of the simple MESFET geometry. The gray shaded area is the semiconductor and the non-shaded region is the insulating substrate. (a) A coarse mesh which does not preserve material interfaces and geometry boundaries. (b) A refined mesh which over-meshes the direction parallel to the interface.

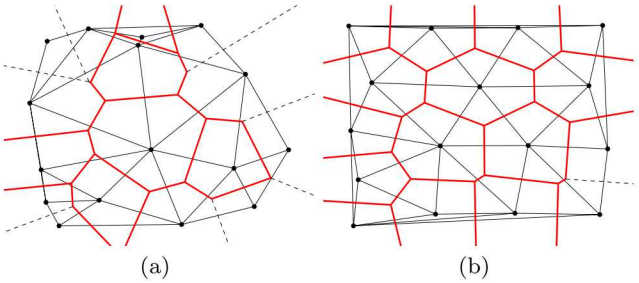


**Fig. 4** The (a) initial DV mesh, which is an input to the CVT algorithm and (b) the resulting DV mesh from the CVT algorithm.

trates (a) the original mesh and (b) the refined mesh in the top left corner of the device. The refined mesh produces conforming Delaunay triangles in both regions as well as Voronoi polygons which preserve geometry boundaries and can preserve material interfaces. This mesh, however, is not optimal for simulating electronic devices because solution variables often change rapidly perpendicular to interfaces. Generating a Delaunay mesh with standard FEM software which preserves material interfaces and geometry boundaries will generate superfluous edges which leads to a very large number of degrees of freedom (DOF).

An alternative to simple mesh refinement could be sophisticated algorithms which ensure that circumcenters do not fall outside of their respective Delaunay elements. One example is the centroidal Voronoi tessellation (CVT) algorithm [36]. In 2D, the CVT algorithm attempts to move the points of the Delaunay triangulation to the centroids of their respective Voronoi polygons. This algorithm can be generalized to higher spatial dimensions. Figure 4 presents an example of the CVT algorithm. Figure 4(a) is the initial DV mesh of a random set of points. The Delaunay mesh points are then moved according to the CVT algorithm to produce Figure 4(b). Clearly, the CVT algorithm produces a quality DV mesh in the interior of the domain. It does not prevent circumcenters from falling outside of the Delaunay triangulation boundary, however. Furthermore, because the algorithm is based upon moving Delaunay mesh nodes, the CVT algorithm will not preserve the original device geometry. Several papers appear in the literature which address these problems. One is a stitching algorithm, which aims to use the CVT algorithm in the interior of the geometry and stitch the resulting mesh onto a boundary conforming and preserving mesh [37–39].

A considerable amount of work exists in DV meshing algorithms specifically designed for semiconductor device geometries. A prominent algorithm which generates 3D Delaunay grids suitable for complex semiconductor device structures was pioneered by Conti, Hitschfeld, and Fichtner [40–42]. An example of a mesh of the simple MESFET geometry generated by an in-house Air Force Research Laboratory, Sensors Directorate ( AFRL/RY) code based on the work of Conti et al. is presented in Figure 5. These meshing algorithms decompose the global device geometry into sub-regions

which can be refined in terms of the mesh. The sub-regions automatically preserve material interfaces and mesh boundaries and the interiors of the sub-regions are allowed to have circumcenters which fall outside of their respective element but still reside inside the sub-region. The commercial device simulator Sentaurus Device, a product of Synopsys, utilizes a separate meshing code which incorporates these algorithms [43]. Further progress on this meshing topic extends the work of Conti et al. to produce meshes conforming to arbitrary boundaries [44,45].

Finally, a discussion on splitting the Voronoi mesh at material interfaces and truncating the Voronoi mesh at geometry boundaries is required. Given that the triangles (2D) or tetrahedra (3D) on material interfaces or mesh boundaries do not have obtuse angles "pointing" towards the interface/boundary, the Voronoi mesh can be properly split or truncated. Figure 6 illustrates material interface truncation on (a) a mesh generated by the algorithm of Conti et al. [40] and (b) a mesh generated by Gmsh [34]. In both instances, the Voronoi cells corresponding to Delaunay nodes on the material interface have edges which are exactly perpendicular to the material interface. The Voronoi edges intersect the primary edges at exactly the circumcenters of the primary edges — the midpoints of the edges. In 3D, the edges of a Voronoi polyhedron intersect at the circumcenters of the Delaunay triangles. The Voronoi diagram at the mesh boundaries uses the same recipe for truncation. The portion of the Voronoi cell which falls outside of the Delaunay mesh, however, is not included in the simulation domain. Figure 7 demonstrates the truncation of the Voronoi diagram at a boundary shaded in gray. The Voronoi edges in the plane of the boundary are drawn as dashed red lines. This boundary could be either a material interface or the end of the Delaunay mesh. If the boundary is a material interface, the Voronoi cells can represent areas corresponding to fluxes across the boundary. In the case of mesh boundaries, the Voronoi edges and cells on the plane can be used for BCs. Both of these cases will be highlighted in Section 4.

The following criteria summarize mesh features useful for semiconductor device simulations which utilize the box integration method.

- The mesh must be Delaunay compliant. No nodes of any primary element fall within any of the circumcircles/circumspheres.
- Both the Delaunay triangulation and the Voronoi diagram should preserve mesh boundaries and material interfaces. In other words, the circumcenters of interior elements should not cross mesh boundaries or material interfaces.

## 3 The System of Nonlinear Equations

The governing equations of the FKT device simulator are Poisson's equation, Ampere's and Faraday's equations, electron continuity, energy conservation, and the lattice heating equation [26]. After real and energy space discretization techniques are applied to the continuous equations, the nonlinear residuals for n-type unipolar devices are

$$\begin{aligned}\mathrm{Pois}_i = &\sum_j \left(\Phi_i^{t+1} - \Phi_j^{t+1}\right) \frac{\varepsilon_{ij} A_{ij}}{L_{ij}} \\ &- q \sum_m \left(N_{D,i,m}^{+} - n_{i,m}^{t+1}\right) V_{i,m} = 0, \end{aligned} \tag{2}$$

$$\begin{aligned}\mathrm{Amp}_i = &\left[E_{\mathrm{rot},i}^{t+1} + \frac{\Phi_{i,0}^{t+1} - \Phi_{i,1}^{t+1}}{L_i} - E_{\mathrm{rot},i}^{t} \right. \\ &\left. - \frac{\Phi_{i,0}^{t} - \Phi_{i,1}^{t}}{L_i}\right] \frac{\varepsilon_i A_i}{\Delta t} - q \sum_m J_{n,i,m}^{t+1} A_{i,m} \\ &- \sum_j H_j^{t+1} L_j = 0, \end{aligned} \tag{3}$$

$$\mathrm{Far}_i = \frac{H_i^{t+1} - H_i^{t}}{\Delta t} \mu_0 A_i + \sum_j E_{\mathrm{rot},j} L_j = 0, \tag{4}$$

$$\begin{aligned}\mathrm{ElCont}_i = &\left[\frac{n_i^{t+1} - n_i^{t}}{\Delta t} + C_i^{n,t+1}\right] V_i \\ &+ \sum_j J_{n,ij}^{t+1} A_{ij} = 0, \end{aligned} \tag{5}$$

$$\begin{aligned}\mathrm{EnCons}_i = &\left[\frac{\mathcal{E}_{n,i}^{t+1} - \mathcal{E}_{n,i}^{t}}{\Delta t} + C_i^{\mathcal{E},t+1}\right] V_i \\ &+ q \sum_j \left(E_j^{t+1} L_j\right) J_{n,ij}^{t+1} A_{ij} + \sum_j S_{n,ij}^{t+1} A_{ij} = 0, \end{aligned} \tag{6}$$

$$\begin{aligned}\mathrm{LattCons}_i = &\rho_i C_{p,i} \frac{T_{L,i}^{t+1} - T_{L,i}^{t}}{\Delta t} V_i - \sum_m C_{i,m}^{\mathcal{E},t+1} V_{i,m} \\ &+ \sum_j \left(T_{L,i}^{t+1} - T_{L,j}^{t+1}\right) \frac{\kappa_{ij} A_{ij}}{L_{ij}} = 0. \end{aligned} \tag{7}$$

Solution variable assignment is discussed in subsequent sections. The terms $N_D^+$, $C^n$, and $C^{\mathcal{E}}$ represent the ionized donor density and the particle and energy collision operators, respectively. Physical constants of Eqns. (2) – (7) include the semiconductor permittivity, $\varepsilon$, the electron charge $q$, the permeability of free space, $\mu_0$, the mass density of the semiconductor, $\rho$, the specific heat

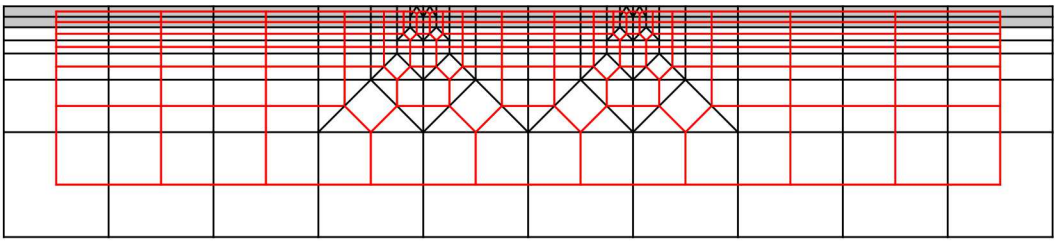

**Fig. 5** The Delaunay triangulation (black lines) and the corresponding polygons of the Voronoi diagram (red lines) of the basic outline of a MESFET. This mesh was generated with an in-house code based upon the work of Conti et al.

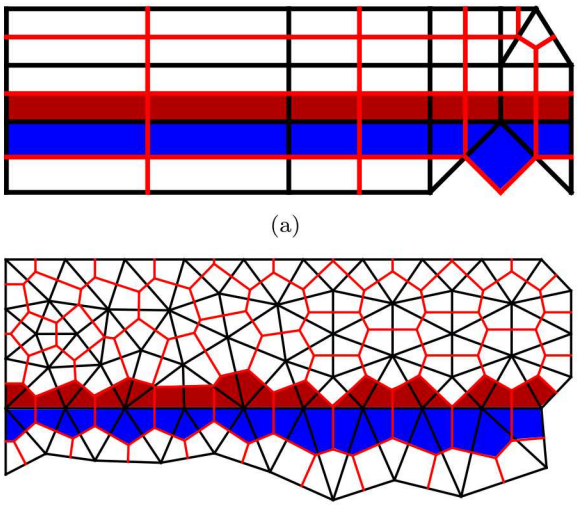


**Fig. 6** Two examples of mesh splitting at material interfaces. In both cases, the primary edges separating the red and blue shaded Voronoi polygons represent the material interface. (a) Material interface Voronoi splitting on a mesh generated by the algorithm of Conti. (b) The same material interface Voronoi splitting on a mesh generated by Gmsh.

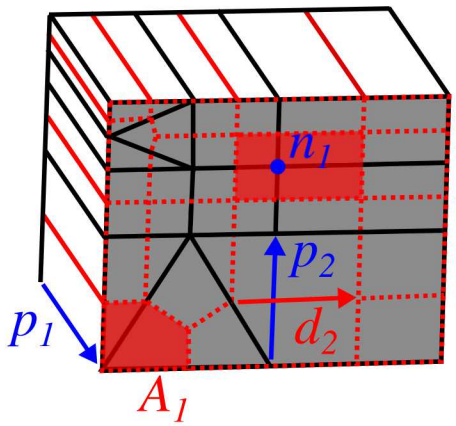


**Fig. 7** An example of Voronoi diagram splitting in 3D. The primary edges are drawn in black and the Voronoi edges are drawn in red. The interface of the Delaunay mesh is shaded in gray. The dashed red lines correspond to the Voronoi cells in the plane of the interface. Two Voronoi cells in the interface are shaded in red.

of the semiconductor, $C_p$, and the thermal conductivity of the semiconductor, $\kappa$. Energy space discretization techniques are presented in detail in [24]. The box integration method [27] is used to discretize divergence operators on the DV mesh. A version of the Scharfetter-Gummel (SG) technique [14,24] is used to discretize the particle fluxes, and the full wave EM is discretized with the DV surface integration (DVSI) technique [46]. Backward Euler time integration is used to discretize temporal derivatives. The index $i$ of the residuals corresponds to specific elements in the DV mesh. Densities, fluxes, and collision operators with the subscript $m$ are associated to unique Fermi distributions at the $i^{\text{th}}$ semiconductor node of the DV mesh. Discrete lengths, areas, and volumes of the mesh are denoted by $L$, $A$, and $V$, respectively and $\Delta t$ represents the time step. The electron number and energy densities (with the time step superscript $t$ removed for brevity) are

$$n_i = \sum_k \mathcal{A}_{ik} \left(k_B T_i\right)^{\alpha_{ik}+1} \mathcal{F}_{\alpha_{ik}} \left(\eta_{\rho,ik}, a_{ik}, b_{ik}\right) \tag{8}$$

$$\mathcal{E}_{n,i} = \sum_k \mathcal{A}_{ik} \left(k_B T_i\right)^{\alpha_{ik}+2} \mathcal{F}_{\alpha_{ik}+1} \left(\eta_{\rho,ik}, a_{ik}, b_{ik}\right), \tag{9}$$

and the discretized particle and kinetic energy flux densities are

$$J_{n,ij} = \sum_k \frac{q\mathcal{D}_{jk}}{L_j} \left(\mathcal{T}_{n,jk}\right)_{\text{ave}} \left[B(\xi_{n,jk}) N_{0,jk} - B(-\xi_{n,jk}) N_{1,jk}\right], \tag{10}$$

$$N_{0(1),jk} = \left(k_B T_{0(1)}\right)^{\beta_{jk}} \mathcal{F}'_{\beta_{jk}} \left(\eta_{J,0(1),jk}, c_{jk}, d_{jk}\right), \tag{11}$$

$$\xi_{n,jk} = \frac{1}{\left(\mathcal{T}_{n,jk}\right)_{\text{ave}}} \left[E_j + \Delta\mathcal{T}_{n,jk}\right] L_j, \tag{12}$$

$$K_{n,ij} = \sum_k \frac{q\mathcal{D}_{jk}}{L_j} \left(\mathcal{T}_{\mathcal{E},jk}\right)_{\text{ave}} \left[B(\xi_{\mathcal{E},jk}) \mathcal{E}_{0,jk} - B(-\xi_{\mathcal{E},jk}) \mathcal{E}_{1,jk}\right], \tag{13}$$

$$\mathcal{E}_{0(1),jk} = \left(k_B T_{0(1)}\right)^{\beta_{jk}+1} \mathcal{F}'_{\beta_{jk}+1}\left(\eta_{J,0(1),jk}, c_{jk}, d_{jk}\right), \tag{14}$$

$$\xi_{\mathcal{E},jk} = \frac{1}{\left(\mathcal{T}_{\mathcal{E},jk}\right)_{\text{ave}}}\left[E_j + \Delta\mathcal{T}_{\mathcal{E},jk}\right] L_j. \tag{15}$$

Here, $B(x) = \frac{x}{\exp x - 1}$ is the Bernoulli function. The $j^{\text{th}}$ primary edge corresponds to the stencil associated to the $i^{\text{th}}$ primary node. The index $k$ corresponds to the piece-wise energy windows used to fit the isosurface integral data [24]. Energy power laws of the form $\mathcal{A}_k\left(\mathcal{E}_k\right)^{\alpha_k}$ and $\mathcal{D}_k\left(\mathcal{E}_k\right)^{\beta_k}$ are used for densities and fluxes, respectively [24]. The functions $\left(\mathcal{T}_{n,jk}\right)_{\text{ave}}$ and $\Delta\mathcal{T}_{n,jk}$ are

$$\Delta\mathcal{T}_{n,jk} = \frac{1}{L_j}\left(\frac{k_B T}{q}\frac{\mathcal{F}_{\beta_{jk}}}{\mathcal{F}'_{\beta_{jk}}}\bigg|_{j,1} - \frac{k_B T}{q}\frac{\mathcal{F}_{\beta_{jk}}}{\mathcal{F}'_{\beta_{jk}}}\bigg|_{j,0}\right), \tag{16}$$

$$\left(\mathcal{T}_{n,jk}\right)_{\text{ave}} = \frac{1}{2}\left(\frac{k_B T}{q}\frac{\mathcal{F}_{\beta_{jk}}}{\mathcal{F}'_{\beta_{jk}}}\bigg|_{j,1} + \frac{k_B T}{q}\frac{\mathcal{F}_{\beta_{jk}}}{\mathcal{F}'_{\beta_{jk}}}\bigg|_{j,0}\right). \tag{17}$$

Here, the notation "$j,0$" represents node zero of the $j^{\text{th}}$ primary edge. The equivalent functions for the kinetic energy flux density are

$$\Delta\mathcal{T}_{\mathcal{E},jk} = \frac{1}{L_j}\left(\frac{k_B T}{q}\frac{\mathcal{F}_{\beta_{jk}+1}}{\mathcal{F}'_{\beta_{jk}+1}}\bigg|_{j,1} - \frac{k_B T}{q}\frac{\mathcal{F}_{\beta_{jk}+1}}{\mathcal{F}'_{\beta_{jk}+1}}\bigg|_{j,0}\right), \tag{18}$$

$$\left(\mathcal{T}_{\mathcal{E},jk}\right)_{\text{ave}} = \frac{1}{2}\left(\frac{k_B T}{q}\frac{\mathcal{F}_{\beta_{jk}+1}}{\mathcal{F}'_{\beta_{jk}+1}}\bigg|_{j,1} + \frac{k_B T}{q}\frac{\mathcal{F}_{\beta_{jk}+1}}{\mathcal{F}'_{\beta_{jk}+1}}\bigg|_{j,0}\right). \tag{19}$$

The incomplete Fermi-Dirac integral and its derivative are

$$\mathcal{F}_\alpha(\eta, a, b) = \int_a^b \frac{\varepsilon^\alpha}{\exp\left(\varepsilon - \eta\right) + 1} d\varepsilon, \tag{20}$$

and

$$\mathcal{F}'_\alpha(\eta, a, b) = \frac{d\mathcal{F}_\alpha}{d\eta} = \alpha\mathcal{F}_{\alpha-1}(\eta, a, b) + \frac{a^\alpha}{\exp\left(\varepsilon - \eta\right) + 1} - \frac{b^\alpha}{\exp\left(\varepsilon - \eta\right) + 1}. \tag{21}$$

The parameters of the Fermi integrals, $\eta$, a, and b, and their relations to FKT solution variables are discussed in [24]. The series expansion method [47] is preferred for the fast numerical evaluation of the incomplete Fermi integral of arbitrary order and parameter. With the definitions

$$J_{0,ijk}\left(T_{p,j}, T_{q,j}\right) = \frac{q\mathcal{D}_{jk}}{L_j}\left(\mathcal{T}_{n,jk}\right)_{\text{ave}}\left(T_{p,j}, T_{q,j}\right) \times B(\xi_{n,jk}\left(T_{p,j}\right))N_{0,jk}\left(T_{p,j}\right), \tag{22}$$

$$J_{1,ijk}\left(T_{p,j}, T_{q,j}\right) = \frac{q\mathcal{D}_{jk}}{L_j}\left(\mathcal{T}_{n,jk}\right)_{\text{ave}}\left(T_{p,j}, T_{q,j}\right) \times B(-\xi_{n,k}\left(T_{p,j}\right))N_{1,jk}\left(T_{p,j}\right), \tag{23}$$

$$K_{0,ijk}\left(T_{p,j}, T_{q,j}\right) = \frac{q\mathcal{D}_{jk}}{L_j}\left(\mathcal{T}_{\mathcal{E},jk}\right)_{\text{ave}}\left(T_{p,j}, T_{q,j}\right) \times B(\xi_{\mathcal{E},jk}\left(T_{p,j}\right))\mathcal{E}_{0,jk}\left(T_{p,j}\right), \tag{24}$$

$$K_{1,ijk}\left(T_{p,j}, T_{q,j}\right) = \frac{q\mathcal{D}_{jk}}{L_j}\left(\mathcal{T}_{\mathcal{E},jk}\right)_{\text{ave}}\left(T_{p,j}, T_{q,j}\right) \times B(-\xi_{\mathcal{E},jk}\left(T_{p,j}\right))\mathcal{E}_{1,jk}\left(T_{p,j}\right), \tag{25}$$

the heat flow and total energy flux densities are

$$\begin{aligned} H_{n,ij} = \sum_k \{ & K_{0,ijk}(T_{j,0}, T_{j,1}) - K_{0,ijk}(T_{j,1}, T_{j,1}) \\ & - (F - \mathcal{E}_c)_{j,0}\left[J_{0,ijk}(T_{j,0}, T_{j,1}) - J_{0,ijk}(T_{j,1}, T_{j,1})\right] \\ & - K_{1,ijk}(T_{j,0}, T_{j,1}) + K_{1,ijk}(T_{j,0}, T_{j,0}) \\ & + (F - \mathcal{E}_c)_{j,1}\left[J_{1,ijk}(T_{j,0}, T_{j,1})\right. \\ & \left. - J_{1,ijk}(T_{j,0}, T_{j,0})\right]\}, \end{aligned} \tag{26}$$

$$S_{n,ij} = K_{n,ij} + H_{n,ij}. \tag{27}$$

The heat flow algorithm is discussed in detail in [23] and applied to complete electronic band structure in [24].

### 3.1 Solution Variables

The solution variables of the discrete nonlinear system of equations are the electric potential $\Phi_i^{t+1}$, rotational electric field vector projection $E_{\text{rot},i}^{t+1}$, magnetic field vector projection $H_i^{t+1}$, the Fermi level relative to the conduction band minimum in each material $(F - \mathcal{E}_c)_i^{t+1}$, the electron temperature $k_B T_i^{t+1}$ of a Fermi distribution, and the lattice temperature $k_B T_{L,i}^{t+1}$. These solution variables are governed by Eqns. (2) – (7), respectively. Derived solution variables required for evaluation of the incomplete Fermi integral, Eqn. 20, are

$$\eta = \frac{F - \mathcal{E}_c}{k_B T}, \tag{28}$$

$$a = \frac{\mathcal{E}_a}{k_B T}, \tag{29}$$

$$b = \frac{\mathcal{E}_b}{k_B T}, \tag{30}$$

where $\mathcal{E}_a$ and $\mathcal{E}_b$ are the bounds of a piece-wise energy window [24]. Assignment of the electron gas solution variables in real and energy space, EM solution variables, and lattice heating variables are next presented.

### *3.1.1 Electron Gases in Real Space*

One or more electron gases are assigned to each Voronoi polygon (2D) or polyhedron (3D) in the DV mesh located in a semiconducting material. If a semiconductor mesh node lies on a material interface, then the Voronoi cell is split into sub-regions. Each sub-region corresponding to a unique material is assigned a separate electron gas. Primary nodes on the boundary of the mesh are truncated in a similar manner. Section 2 provided a discussion on material interface and mesh boundary splitting of the Voronoi diagram.

Figure 8(a) presents an example of a DV mesh on which electron gases are assigned. Three Voronoi polygons are drawn in Figure 8(b). The Voronoi polygon associated to gas A is completely enclosed in material 2 and therefore the entire polygon shaded in red represents the volume of the gas. Because gas B is associated to a node on the boundary of the mesh, the Voronoi polygon is truncated at the boundary. Node C is an important case in semiconductor device meshes. Because this mesh node resides on a material interface, it receives separate gases associated to the two unique materials. The Voronoi volume of gas C2 (the gas associated to material 2) and the Voronoi volume of gas C3 (the gas associated to material 3) are distinguished with different shading in Figure 8(b). This procedure generalizes to interfaces of an arbitrary number of materials.

### *3.1.2 Electron Gases in Energy Space*

The band structure of a bulk semiconductor is incorporated into the FKT device simulator through piece-wise energy power law fits of the isosurface integrals [24]. For example, the power law fits are used to calculate the electron density and energy density, Eqns. (8) and (9). These densities are associated to a sub-region of the Voronoi cell corresponding to a unique material as described in the previous section.

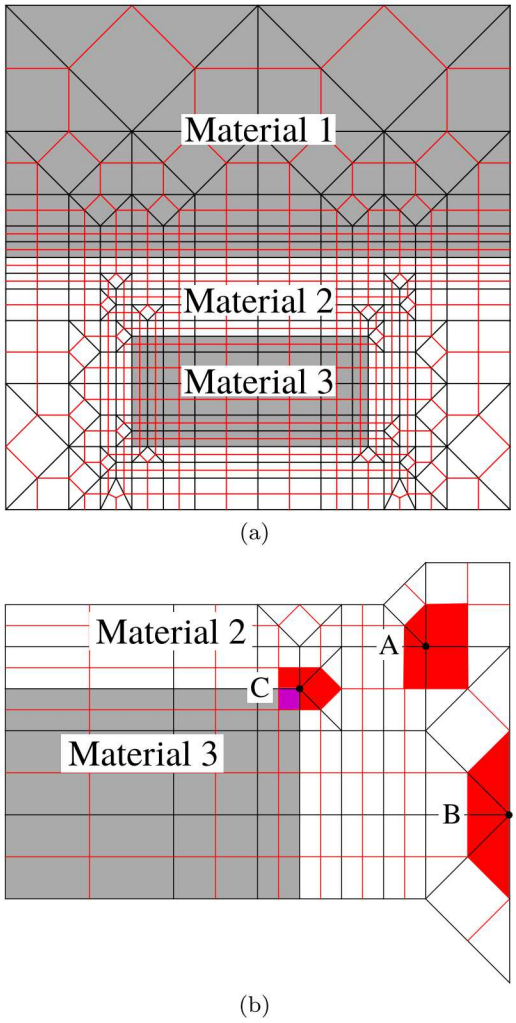


**Fig. 8** (a) An example of a device mesh generated by the Sentaurus meshing tool. (b) An illustration of the electron gases assigned to unique Voronoi polygons in the DV mesh.

The energy space corresponding to an electron gas in a unique material can further be discretized into multiple Fermi distributions. Typically, valleys in the semiconductor band structure are assigned separate distribution functions. Scattering between the distributions is calculated with the collision operators $C^n$ and $C^{\mathcal{E}}$ discussed in detail in [24]. Figure 9 illustrates a panel diagram and the density of states (DOS) isosurface integral of wurtzite GaN [26]. The band structure was calculated with the empirical pseudopotential method (EPM) [48]. In the example in Figure 9, only the first $\Gamma$-valley is included in the DOS calculation and the energy space of the valley is split into two separate Fermi distributions labeled $\Gamma_1$ and $\Gamma_2$. The separation of the first $\Gamma$-valley into two distinct Fermi distributions yields two sets of solution variables, $F - \mathcal{E}_c$ and $k_B T$, at each semiconductor mesh node. Real space transport only occurs between distributions occupying the same regions of en-

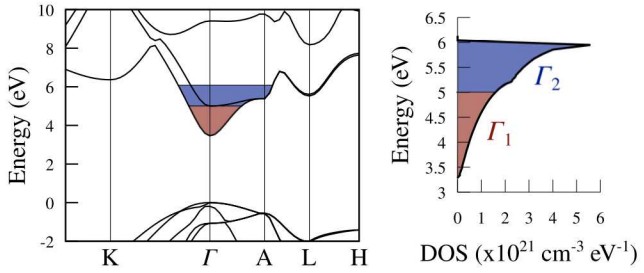


**Fig. 9** The (left) panel diagram of wurtzite GaN and (right) corresponding DOS isosurface integral of the first $\Gamma$-valley. The energy space of the first $\Gamma$-valley is split into two separate Fermi distributions. Therefore, the energy space of each electron gas in distinct real space sub-regions in the semiconductor are approximated with two Fermi distributions.

ergy space. Therefore, there is no particle flux between the $\Gamma_1$ and $\Gamma_2$ distributions. Rather, particles can drift and diffuse between $\Gamma_1$ at mesh node 1 and $\Gamma_1$ at mesh node 2 and then scatter from $\Gamma_1$ to $\Gamma_2$ at mesh node 2. The same is true for energy transport.

### *3.1.3 EM Solution Variables*

The solution variables corresponding to full wave EM are $\Phi_i$, $E_{\text{rot},i}$ and $H_i$. Electric potential solution variables are assigned to all primary nodes of the DV mesh that are not vacuum. The rotational electric field vector projections are defined on the primary edges of the DV mesh and magnetic field vector projections are defined on the dual edges of the DV mesh. A derived solution variable is the total electric field. On the $j^{\text{th}}$ primary edge, the total electric field is

$$E_j = E_{\text{rot},j} + \frac{\Phi_{j,0} - \Phi_{j,1}}{L_j}, \tag{31}$$

where the subscript $j,0$ corresponds to node zero of the primary edge. The primary edge points from node 0 to 1. A complete discussion of the full wave EM discretization, DVSI, is presented in [46].

### *3.1.4 Lattice Heating Solution Variables*

The solution variable corresponding to lattice heating in semiconductor devices is $k_B T_{L,i}^{t+1}$. The lattice temperature solution variables are assigned to all thermal materials in the device. Examples of non-thermal materials in the device include dielectrics like air which are included between metal contacts at the tops of devices.

## 3.2 The Nonlinear Solver: Newton's Method

The nonlinear system, Eqns. (2) – (27), is solved with Newton's method. The system consists of $N_\Phi$ electric potential variables, $N_F$ electron relative Fermi levels, $N_T$ electron temperatures, and $N_{TL}$ lattice temperatures. If full wave EM is included in the device simulation, there are an additional $N_E$ rotational electric field vector projection solution variables and $N_H$ magnetic field vector projection solution variables.

A linear system is solved at each Newton iteration. The linear system is comprised of the residuals $\text{Pois}_i$, $\text{Amp}_i$, $\text{Far}_i$, $\text{ElCont}_i$, $\text{EnCons}_i$, and $\text{LattCons}_i$. With this arrangement, the general Newton linear system is

$$\begin{bmatrix} \frac{\partial \text{Pois}_1}{\partial \Phi_1} & \frac{\partial \text{Pois}_1}{\partial \Phi_2} & \cdots & \frac{\partial \text{Pois}_1}{\partial k_B T_{L,N_{TL}}} \\ \frac{\partial \text{Pois}_2}{\partial \Phi_1} & \frac{\partial \text{Pois}_2}{\partial \Phi_2} & \cdots & \frac{\partial \text{Pois}_2}{\partial k_B T_{L,N_{TL}}} \\ \vdots & & \ddots & \vdots \\ \frac{\partial \text{LattCons}_{N_{TL}}}{k_B T_{L,1}} & \frac{\partial \text{LattCons}_{N_{TL}}}{k_B T_{L,2}} & \cdots & \frac{\partial \text{LattCons}_{N_{TL}}}{k_B T_{L,N_{TL}}} \end{bmatrix} \times \begin{bmatrix} \Delta\Phi_1 \\ \Delta\Phi_2 \\ \vdots \\ \Delta k_B T_{L,N_{TL}} \end{bmatrix} = - \begin{bmatrix} \text{Pois}_1 \\ \text{Pois}_2 \\ \vdots \\ \text{LattCons}_{N_{TL}} \end{bmatrix}. \tag{32}$$

The linear systems corresponding to specific solvers in the FKT device simulation framework are described in the following.

## 3.3 Solve Types

The solve types of the device simulator are grouped into three distinct classes: Equilibrium, static, and transient solves. The Newton linear system corresponding to a specific device solve is presented in block matrix form. For example, the matrix corresponding to the partial derivative of the $i^{\text{th}}$ Poisson residual with respect to the $j^{\text{th}}$ electric potential solution variable is $\frac{\partial \text{Pois}_i}{\partial \Phi_j}$. The $i^{\text{th}}$ diagonal of this matrix is

$$\frac{\partial \text{Pois}_i}{\partial \Phi_i} = \sum_j \frac{\varepsilon_{ij} A_{ij}}{L_{ij}}. \tag{33}$$

The derivative of the $i^{\text{th}}$ Poisson residual with respect to the $j^{\text{th}}$ Fermi level solution variable is

$$\frac{\partial \text{Pois}_i}{\partial (F - \mathcal{E}_c)_j} = q \sum_m \frac{\partial n_{i,m}^{t+1}}{\partial (F - \mathcal{E}_c)_j} V_{i,m}. \tag{34}$$

This Jacobian element requires partial derivatives of the densities with respect to the relative Fermi levels. The numerical routine which calculates the incomplete Fermi integrals also returns the derivative of the Fermi integrals for these purposes.

### 3.4 Equilibrium Solve

The equilibrium solve is the first component of the device simulation work-flow. This produces the electric potential and electron relative Fermi level profiles in thermal equilibrium. Only Poisson's equation, Eqn. (2), is solved to produce the thermal equilibrium solution profiles. The Newton linear system of this solve is

$$\left[\, \frac{\partial \mathrm{Pois}_i}{\partial \Phi_j} \,\right] \left[\, \Delta \Phi_j \,\right] = - \left[\, \mathrm{Pois}_i \,\right]. \tag{35}$$

Because the conduction band, $\mathcal{E}_c$, will vary across the device in thermal equilibrium, the relative Fermi level solution variable, $F - \mathcal{E}_c$, must also be updated after each Newton iteration. This can be accomplished by amending the diagonals of the Jacobian to be

$$\begin{aligned} \frac{\partial \mathrm{Pois}_i}{\partial \Phi_i} &= \sum_j \frac{\varepsilon_{ij} A_{ij}}{L_{ij}} + q \sum_m \frac{\partial n_{i,m}^{t+1}}{\partial \Phi_i} V_{i,m} \\ &= \sum_j \frac{\varepsilon_{ij} A_{ij}}{L_{ij}} - q \sum_m \frac{\partial n_{i,m}^{t+1}}{\partial (\mathcal{E}_c)_i} V_{i,m} \\ &= \sum_j \frac{\varepsilon_{ij} A_{ij}}{L_{ij}} + q \sum_m \frac{\partial n_{i,m}^{t+1}}{\partial (F - \mathcal{E}_c)_i} V_{i,m}. \end{aligned} \tag{36}$$

The relation $\mathcal{E}_c = -\chi_e - \Phi$, where $\chi_e$ is the electron affinity of the semiconducting material, dictates that a positive change in the electric potential corresponds to a negative change in the conduction band. Furthermore, the electron Fermi level, $F$, is spatially constant at thermal equilibrium which allows for the final substitution in Eqn. (36).

After the Poisson stage of the thermal equilibrium solve, the rest of the steady-state equations are added one at a time to allow all solution variables to relax to their numerical thermal equilibrium. The Newton linear system of the final equilibrium stage, comprised of the residuals $\mathrm{Pois}_i$, $\mathrm{ElCont}_i$, $\mathrm{EnCons}_i$, and $\mathrm{LattCons}_i$, is shown in Eqn. (37). The additional stages of the thermal equilibrium solves do not drastically change the electric potential or relative Fermi level solution variables.

### 3.5 Static Solve

The next solve in the semiconductor device simulation work-flow is the static or steady-state solve. Typically, an external voltage or current bias is applied to metal contacts to produce steady-state current flow. The static solver computes steady-state data including the current-voltage (I-V) family and transconductance. The quiescent bias of a transistor is also calculated with the static solver.

As described previously, a linear system is solved at each Newton iteration in order to update the FKT device simulation solution variables. The linear system of the $m^{\mathrm{th}}$ static Newton iteration is

$$\begin{bmatrix} \frac{\partial \mathrm{Pois}_i}{\partial \Phi_j} & \frac{\partial \mathrm{Pois}_i}{\partial (F-\mathcal{E}_c)_j} & \frac{\partial \mathrm{Pois}_i}{\partial k_B T_j} & \frac{\partial \mathrm{Pois}_i}{\partial k_B T_{L,j}} \\ \frac{\partial \mathrm{ElCont}_i}{\partial \Phi_j} & \frac{\partial \mathrm{ElCont}_i}{\partial (F-\mathcal{E}_c)_j} & \frac{\partial \mathrm{ElCont}_i}{\partial k_B T_j} & \frac{\partial \mathrm{ElCont}_i}{\partial k_B T_{L,j}} \\ \frac{\partial \mathrm{EnCons}_i}{\partial \Phi_j} & \frac{\partial \mathrm{EnCons}_i}{\partial (F-\mathcal{E}_c)_j} & \frac{\partial \mathrm{EnCons}_i}{\partial k_B T_j} & \frac{\partial \mathrm{EnCons}_i}{\partial k_B T_{L,j}} \\ 0 & \frac{\partial \mathrm{LattCons}_i}{\partial (F-E_c)_j} & \frac{\partial \mathrm{LattCons}_i}{\partial k_B T_j} & \frac{\partial \mathrm{LattCons}_i}{\partial k_B T_{L,j}} \end{bmatrix} \times \begin{bmatrix} \Delta \Phi_j \\ \Delta (F - \mathcal{E}_c)_j \\ \Delta k_B T_j \\ \Delta k_B T_{L,j} \end{bmatrix} = - \begin{bmatrix} \mathrm{Pois}_i \\ \mathrm{ElCont}_i \\ \mathrm{EnCons}_i \\ \mathrm{LattCons}_i \end{bmatrix}. \tag{37}$$

The static FKT device simulation equations include Eqns. (2), (5), (6), and (7) with all time derivatives set to zero, i.e., $\frac{\partial}{\partial t} \to 0$. The Jacobian matrix, Eqn. (37), is more complex than the equilibrium Jacobian matrix. For example, the middle diagonal matrix element requires the partial derivative of the collision operator and the particle flux with respect to the relative Fermi level solution variable. This Jacobian matrix element is

$$\frac{\partial \mathrm{ElCont}_i}{\partial (F - \mathcal{E}_c)_j} = \frac{\partial C_i^{n,t+1}}{\partial (F - \mathcal{E}_c)_j} V_i + \sum_j \frac{\partial J_{n,ij}^{t+1}}{\partial (F - \mathcal{E}_c)_j} A_{ij}. \tag{38}$$

Derivatives of incomplete Fermi integrals are required for evaluating this Jacobian matrix element. The particle flux is exponentially dependent on ratios of Fermi integrals making this matrix element highly nonlinear.

### 3.6 Quasi-Static Solve

After the quiescent bias of the device is calculated by the static solve, the quasi-static solve can be used to simulate the RF response without the inclusion of full wave EM. The RF response metrics of transistors include small-signal S-Parameters. These simulated parameters computed across a broad frequency range can be very useful to circuit designers for impedance matching at input and output ports in commercial software including Advanced Design System (ADS) [49].

The linear system of the $m^{\mathrm{th}}$ Newton iteration of the quasi-static simulation retains the same form as Eqn. (37). However, because the time derivatives are now included in Eqns. (2), (5), (6), and (7), the Jacobian matrix is different. As an example, the middle diagonal

element of the quasi-static Jacobian matrix is

$$\frac{\partial \mathrm{ElCont}_i}{\partial (F-\mathcal{E}_c)_j} = \left( \frac{\partial n_i^{t+1}}{\partial (F-\mathcal{E}_c)_j} \frac{1}{\Delta t} + \frac{\partial C_i^{n,t+1}}{\partial (F-\mathcal{E}_c)_j} \right) V_i + \sum_j \frac{\partial J_{n,ij}^{t+1}}{\partial (F-\mathcal{E}_c)_j} A_{ij}. \quad (39)$$

The time step $\Delta t$ is typically chosen according to the driving frequency of the electronic device simulation. A standard choice is $\Delta t = 1/(100 \times f_0)$, where $f_0$ is the fundamental frequency of the device simulation.

### 3.7 Full Wave Solve

Full wave and hot electron effects are captured in an electronic device simulation by solving Eqns. (2) – (7). This solver can produce simulated S-Parameters which reflect the high frequency parasitics in an electronic device. The Newton linear system corresponding to a full wave FKT device simulation is

$$\begin{bmatrix} \frac{\partial \mathrm{Pois}_i}{\partial \Phi_j} & 0 & 0 & \frac{\partial \mathrm{Pois}_i}{\partial (F-\mathcal{E}_c)_j} & \frac{\partial \mathrm{Pois}_i}{\partial k_B T_j} & \frac{\partial \mathrm{Pois}_i}{\partial k_B T_{L,j}} \\ \frac{\partial \mathrm{Amp}_i}{\partial \Phi_j} & \frac{\partial \mathrm{Amp}_i}{\partial E_{\mathrm{rot},j}} & \frac{\partial \mathrm{Amp}_i}{\partial H_j} & \frac{\partial \mathrm{Amp}_i}{\partial (F-\mathcal{E}_c)_j} & \frac{\partial \mathrm{Amp}_i}{\partial k_B T_j} & 0 \\ 0 & \frac{\partial \mathrm{Far}_i}{\partial E_{\mathrm{rot},j}} & \frac{\partial \mathrm{Far}_i}{\partial H_j} & 0 & 0 & 0 \\ \frac{\partial \mathrm{ElC}_i}{\partial \Phi_j} & \frac{\partial \mathrm{ElC}_i}{\partial E_{\mathrm{rot},j}} & 0 & \frac{\partial \mathrm{ElC}_i}{\partial (F-\mathcal{E}_c)_j} & \frac{\partial \mathrm{ElC}_i}{\partial k_B T_j} & \frac{\partial \mathrm{ElC}_i}{\partial k_B T_{L,j}} \\ \frac{\partial \mathrm{EnC}_i}{\partial \Phi_j} & \frac{\partial \mathrm{EnC}_i}{\partial E_{\mathrm{rot},j}} & 0 & \frac{\partial \mathrm{EnC}_i}{\partial (F-\mathcal{E}_c)_j} & \frac{\partial \mathrm{EnC}_i}{\partial k_B T_j} & \frac{\partial \mathrm{EnC}_i}{\partial k_B T_{L,j}} \\ 0 & 0 & 0 & \frac{\partial \mathrm{LC}_i}{\partial (F-\mathcal{E}_c)_j} & \frac{\partial \mathrm{LC}_i}{\partial k_B T_j} & \frac{\partial \mathrm{LC}_i}{\partial k_B T_{L,j}} \end{bmatrix} \times \begin{bmatrix} \Delta \Phi_j \\ \Delta E_{\mathrm{rot},j} \\ \Delta H_j \\ \Delta (F-\mathcal{E}_c)_j \\ \Delta k_B T_j \\ \Delta k_B T_{L,j} \end{bmatrix} = - \begin{bmatrix} \mathrm{Pois}_i \\ \mathrm{Amp}_i \\ \mathrm{Far}_i \\ \mathrm{ElC}_i \\ \mathrm{EnC}_i \\ \mathrm{LC}_i \end{bmatrix} \quad (40)$$

Here, the electron continuity, energy conservation, and lattice heating residuals are renamed to $\mathrm{ElC}_i$, $\mathrm{EnC}_i$, and $\mathrm{LC}_i$, respectively. Full wave simulations use the same choice of time step as quasi-static simulations.

## 4 Boundary Conditions

A list of the BCs required for electronic device simulations is presented in Table 1. Typical BCs include metal contacts and port BCs used to provide or absorb EM energy.

### 4.1 Ohmic Metal Contact

An essential metal BC found in almost every semiconductor device simulation is the Ohmic contact. Charge neutrality is enforced at a distribution on an interface between a semiconductor and an Ohmic contact. The solution variable $F - \mathcal{E}_c$ of a charge distribution on an Ohmic contact interface is fixed to the charge neutral value $(F - \mathcal{E}_c)_{\mathrm{CN}}$ and, for the perfect electrical conductor approximation, the contact maintains the electric potential $\Phi_{\mathrm{CN}} + V_a$. Here, $V_a$ is a voltage applied to the Ohmic contact. The charge neutral quantities are determined by the numerical solution of

$$\mathrm{Pois}_i|_{\mathrm{ohm.}} \equiv \sum_m \left( N_{D,i,m}^+ - n_{i,m}^{t+1} \right) V_{i,m} = 0, \quad (41)$$

and the assignment

$$\Phi_{\mathrm{CN}} = -\chi_e + \Phi_M + (F - \mathcal{E}_c)_{\mathrm{CN}}. \quad (42)$$

Here, the electron affinity, $\chi_e$, and the work-function, $\Phi_M$, are properties of the semiconductor and metal, respectively.

### 4.2 Lattice Heat Absorbing Boundary Condition

The heat absorbing (HA) BC is meant to emulate lattice heat flow out of the device domain. Without this BC, the simulated devices will heat up to nonphysical levels. Outgoing lattice heat flow is represented by the outward lattice temperature gradient $(\nabla T_L)_{\mathrm{HA}}$ on a boundary mesh node. The area of the gradient flux corresponds to the in-plane Voronoi polygons associated to primary nodes on the mesh boundary. In Figure 7, the gradient flux area associated to the primary node labeled $n_1$ is shaded in red. The total HA BC is

$$\mathrm{LattCons}_i|_{\mathrm{HA}} \equiv \left[ \rho_i C_{p,i} \frac{T_{L,i}^{t+1} - T_{L,i}^t}{\Delta t} - \sum_i C_i^{\mathcal{E},t+1} \right] V_i + \sum_j \left( T_{L,i}^{t+1} - T_{L,j}^{t+1} \right) \frac{\kappa_{ij} A_{ij}}{L_{ij}} + \left[ \hat{n} \cdot (\nabla T_L)\, \kappa A \right]_{\mathrm{HA}} = 0. \quad (43)$$

Here, $\hat{n}$ represents the normal of the mesh boundary. The lattice temperature gradients at the mesh nodes of the HA boundary are reconstructed from the vector projections of the lattice temperature gradients onto the primary edges associated to the mesh nodes.

### 4.3 Quasi-Static AC Impedance Boundary Condition

The quasi-static solver is suitable for lower frequency simulations where full wave effects are negligible. In order to calculate useful quantities with the quasi-static solver, the AC impedance must be used as a termination opposite the excitation contact. The AC impedance BC

| B.C. | $\Phi$ | $E_{\text{rot}}$ | $H$ | $F - \mathcal{E}_c$ | $k_B T$ | $k_B T_L$ |
|---|---|---|---|---|---|---|
| Ohmic | $\Phi_{\text{CN}} + V_a$ | 0 | 0 | $(F - \mathcal{E}_c)_{\text{CN}}$ | $k_B T_L$ | Soln. |
| Schottky | $\Phi_{\text{SB}} + V_a$ | 0 | 0 | Soln. | Soln. | Soln. |
| Lattice heat absorbing | Soln. | Soln. | Soln. | Soln. | Soln. | Soln. |
| AC impedance (Ohmic) | $\Phi_{\text{ACI}}^{t+1}$ | 0 | 0 | $(F - \mathcal{E}_c)_{\text{CN}}$ | $k_B T_L$ | Soln. |
| AC impedance (Schottky) | $\Phi_{\text{ACI}}^{t+1}$ | 0 | 0 | Soln. | Soln. | Soln. |
| Full wave voltage | Soln. | 0 | Soln. | Soln. | Soln. | Soln. |
| Full wave impedance | Soln. | Soln. | $H_{\text{imp}}$ | Soln. | Soln. | Soln. |

**Table 1** A list of semiconductor device simulation BCs.

is defined on metal contacts in the quasi-static solver. The integrated current flowing into the AC impedance contact is

$$i^{t+1} = \sum_k J_k^{t+1} A_k. \tag{44}$$

Here, $J_k$ represents the particle flux density on the $k^{\text{th}}$ primary edge pointing into the AC impedance metal contact. The area $A_k$ is that of the in-plane Voronoi polygon associated to the primary edge. In Figure 7, the area of the in-plane Voronoi polygon labeled $A_1$ corresponds to the particle flux vector projection defined on the primary edge $p_1$. The integrated current on this BC specifies a Dirichlet condition on the metal contact's potential via Ohm's law, i.e.,

$$\Phi_i^{t+1}\big|_{\text{ACI}} = Z_{\text{ACI}} i_{\text{ACI}}^{t+1}, \tag{45}$$

where $i_{\text{ACI}}^{t+1} \equiv i^{t+1} - i^{t=0}$ represents only the AC component of the integrated current. This approximates the effects of a bias tee, which is typically used for measuring dynamic quantities such as S-Parameters.

### 4.4 Full Wave Voltage Port

The voltage BC is a specific case of the port BC in which EM energy enters the full wave solver. The voltage port connects two metal contacts in the device under test (DUT). The electric field in the voltage port is strictly irrotational, i.e., $E_{\text{rot},i} = 0$. Ampere's law is solved on voltage port primary edges. The BC is

$$\text{Amp}_i|_{\text{volt.}} \equiv \left[E_{i,\text{irr}}^{t+1} - E_{i,\text{irr}}^{t}\right] \frac{\varepsilon_i A_i}{\Delta t} - q \sum_m J_{n,im}^{t+1} A_{im} - \sum_j H_j^{t+1} L_j = 0. \tag{46}$$

Here, the irrotational electric field is $E_{i,\text{irr}}^{t+1} = \frac{\Phi_{i,0} - \Phi_{i,1}}{L_i}$ where the subscript $i, 0$ corresponds to node zero of the $i^{\text{th}}$ primary edge. The primary edge points from node 0 to 1. This BC serves as the governing equation for the magnetic field defined on the $i^{\text{th}}$ in-plane dual edge associated to a primary edge on the boundary. In Figure 7, the in-plane dual edge labeled $d_2$ corresponds to the primary edge $p_2$ on the voltage BC. The magnetic field vector projection defined on this in-plane dual edge is included in the line integral of Eqn. (46).

### 4.5 Full Wave AC Impedance Port

The full wave AC impedance (FWACI) BC is an energy sink port BC connecting two metal contacts. The magnetic field $H_{\text{FWACI}}$ is defined on an in-plane dual edge associated to a primary edge on the boundary. The definition of the in-plane dual edge associated to the primary edge in the BC is the same as the full wave voltage port BC. The magnetic field is equal to the total electric field defined on the primary edge divided by the boundary's impedance $Z_{\text{FWACI}}$. The BC is

$$\text{FWACI}_i \equiv E_i^{t+1} - E_i^{t=0} - Z_{\text{FWACI}} \left(H_{i,\text{FWACI}}^{t+1} - H_{i,\text{FWACI}}^{t=0}\right) = 0, \tag{47}$$

In a manner similar to the quasi-static AC impedance BC, the subtraction of the solutions calculated at the first time step ensures that the BC only affects the AC components of the solution variables.

### 4.6 Heterojunctions and Thermionic Emission Boundaries

As outlined in Section 3.1.1, one or more electron gases are assigned to semiconductor mesh nodes residing on heterojunctions. Figure 10 illustrates a thermal equilibrium band diagram across a heterojunction of two semiconductors. In this example, each electron gas is approximated with a single Fermi distribution in energy space. Because the two materials have different electron affinities, there is a discontinuity in the conduction band across the heterojunction and thermionic emission is used to calculate real space transport across the discontinuity. With both distributions' Fermi levels referenced to the higher conduction band, the particle

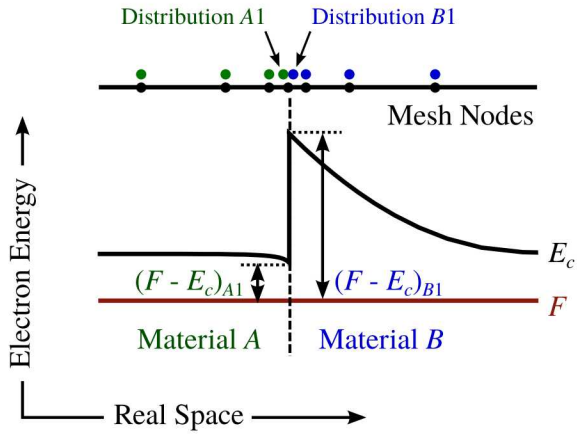


**Fig. 10** The thermal equilibrium band diagram across a two material heterojunction. The electron affinity of material A is greater than material B's electron affinity. The relative Fermi level solution variables are illustrated for each electron gas at the heterojunction.

flux and kinetic energy flux density thermionic emissions from semiconductor node 1 to semiconductor node 2 are

$$J_{n,TE}^{1\to2}(T_1) = \frac{1}{2\pi^2}\frac{m^*}{\hbar^3}\left(k_B T_1\right)^2 \times \int_0^\infty d\varepsilon_z \ln\left[1+\exp\left(\tilde{\eta}_1 - \varepsilon_z\right)\right], \tag{48}$$

and

$$K_{n,TE}^{1\to2}(T_1) = \frac{1}{\pi^2}\frac{m^*}{\hbar^3}\left(k_B T_1\right)^3 \times \int_0^\infty d\varepsilon_z \varepsilon_z \ln\left[1+\exp\left(\tilde{\eta}_1 - \varepsilon_z\right)\right], \tag{49}$$

with the parameter

$$\tilde{\eta}_1 = \frac{\left(F-\mathcal{E}_c\right)_1 + \mathcal{E}_{c,1} - \mathcal{E}_{c,\text{high}}}{k_B T_1}. \tag{50}$$

Here, $m^*$ is the effective mass of the semiconductor with the lower electron affinity and $\hbar$ is the Planck constant. A numerical quadrature routine is required to evaluate Eqns. (48) and (49). The high side conduction band edge, $\mathcal{E}_{c,\text{high}}$, is associated to the charge distribution in the material with the smaller electron affinity at the heterojunction. The total thermionic emission particle, kinetic energy, heat, and total energy flux densities are

$$J_{n,TE} = J_{n,TE}^{1\to2}(T_1) - J_{n,TE}^{2\to1}(T_2), \tag{51}$$

$$K_{n,TE} = K_{n,TE}^{1\to2}(T_1) - K_{n,TE}^{2\to1}(T_2), \tag{52}$$

$$\begin{aligned} H_{n,TE} = {} & K_{n,TE}^{1\to2}(T_1) - K_{n,TE}^{1\to2}(T_2) \\ & - \left(F-\mathcal{E}_{c,\text{high}}\right)_1 \left[J_{n,TE}^{1\to2}(T_1) - J_{n,TE}^{1\to2}(T_2)\right] \\ & - K_{n,TE}^{2\to1}(T_2) + K_{n,TE}^{2\to1}(T_1) \\ & + \left(F-\mathcal{E}_{c,\text{high}}\right)_2 \left[J_{n,TE}^{2\to1}(T_2) - J_{n,TE}^{2\to1}(T_1)\right], \end{aligned} \tag{53}$$

and

$$S_{n,TE} = K_{n,TE} + H_{n,TE}. \tag{54}$$

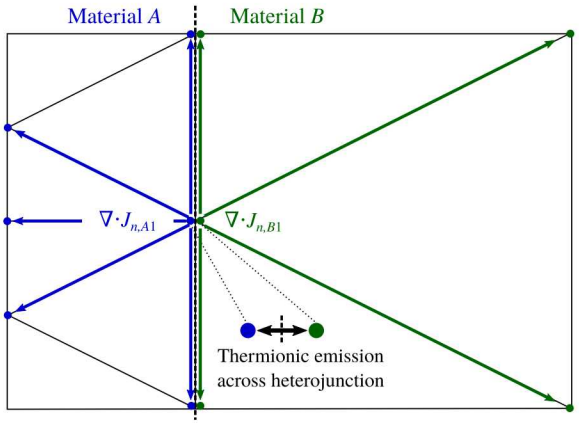


**Fig. 11** An example of the particle flux divergences associated to two electron gases at a heterojunction. BTE particle fluxes are calculated between two electron gases in the same semiconductor.

The thermionic particle flux and total energy flux densities are added to the electron continuity and energy conservation divergences, Eqns. (5) and (6). Figure 11 illustrates the particle divergence for the two unique charge distributions defined on a heterojunction mesh node. There is only a BTE particle flux ($J_{n,ij}$ and $K_{n,ij}$) between charges associated to the same material. Thermionic emission connects the two charge distributions at the heterojunction. With charge distributions $A1$ and $B1$ at the heterojunction mesh node, the electron continuity and energy conservation equations for both distributions are

$$\text{ElCont}_{A1}|_{\text{HJ}} \equiv \left(\frac{n_{A1}^{t+1} - n_{A1}^{t}}{\Delta t} + C_{A1}^{n,t+1}\right) V_{A1} + \sum_j J_{n,A1j}^{t+1} A_{A1j} + J_{n,TE}^{t+1} A_{TE} = 0, \tag{55}$$

$$\text{ElCont}_{B1}|_{\text{HJ}} \equiv \left(\frac{n_{B1}^{t+1} - n_{B1}^{t}}{\Delta t} + C_{B1}^{n,t+1}\right) V_{B1} + \sum_j J_{n,B1j}^{t+1} A_{B1j} - J_{n,TE}^{t+1} A_{TE} = 0, \tag{56}$$

$$\begin{aligned}\mathrm{EnCons}_{A1}|_{\mathrm{HJ}} \equiv & \left(\frac{\mathcal{E}_{n,A1}^{t+1}-\mathcal{E}_{n,A1}^{t}}{\Delta t}+C_{A1}^{\mathcal{E},t+1}\right)V_{A1} \\ & +q\sum_{j}\left(E_{j}^{t+1}L_{j}\right)J_{n,ij}^{t+1}A_{A1j} \\ & +\sum_{j}S_{n,A1j}^{t+1}A_{ij}+S_{n,TE}^{t+1}A_{TE} \\ & +\mathcal{E}_{\mathrm{pot}}J_{n,TE}^{t+1}A_{TE}=0. \end{aligned} \tag{57}$$

$$\begin{aligned}\mathrm{EnCons}_{B1}|_{\mathrm{HJ}} \equiv & \left(\frac{\mathcal{E}_{n,B1}^{t+1}-\mathcal{E}_{n,B1}^{t}}{\Delta t}+C_{B1}^{\mathcal{E},t+1}\right)V_{B1} \\ & +q\sum_{j}\left(E_{j}^{t+1}L_{j}\right)J_{n,B1j}^{t+1}A_{B1j} \\ & +\sum_{j}S_{n,B1j}^{t+1}A_{ij}-S_{n,TE}^{t+1}A_{TE}=0. \end{aligned} \tag{58}$$

Here, HJ refers to the heterojunction. The last term in Eqn. (57) represents the potential energy required to overcome the barrier $\mathcal{E}_{\mathrm{pot}}=\chi_A-\chi_B$ with $\chi_A>\chi_B$. The area $A_{TE}$ corresponds to the Voronoi polygon in the heterojunction plane associated to the primary node on the interface. In Figure 7, the thermionic emission flux area corresponding to the heterojunction mesh node labeled $n_1$ is shaded in red.

### 4.7 Schottky Metal Contact

Another important BC is the rectifying Schottky metal contact. This metal-semiconductor interface is a special type of heterojunction. The important characteristic of the BC is the Schottky barrier $\Phi_{\mathrm{SB}}$. With no applied bias, the solution variable $F-\mathcal{E}_c$ of a charge distribution at this interface equals $-q\Phi_{\mathrm{SB}}$. In the typical way, an applied bias which raises the Fermi level and conduction band minimum in the Schottky metal will increase the potential barrier of the metal-semiconductor interface. An applied bias which lowers the Fermi level and conduction band minimum will decrease the potential barrier. The energy between the metal Fermi level and the semiconductor conduction band minimum remains constant. Transport across the discontinuity caused by the Schottky barrier is calculated with thermionic emission. The energy $-q\Phi_{\mathrm{SB}}$ and the lattice temperature $k_BT_L$ are used to compute the thermionic emission from the metal into the semiconductor.

## 5 Mesh Convergence of the Discrete FKT Equations

The mesh convergence of the discrete FKT device simulation equations is investigated. This numerical characteristic provides insight into how the errors of the device simulation solution variables converge with mesh refinement. Simulation of large electronic devices requires meshing strategies in order to yield accurate results without insurmountable computational demands.

Convergence of the discrete FKT equations is quantified by evaluating the $i^{\mathrm{th}}$ relative $L^2$ error

$$\epsilon_{ik}=\sqrt{\frac{\sum_{j}w_j\left[\tilde{u}_{ij,k}-u_{ij,k}\right]^2}{\sum_{j}w_ju_{ij,k}^2}}, \tag{59}$$

on a series of meshes. Here, $\tilde{u}_{ij,k}$ and $u_{ij,k}$ are the $i^{\mathrm{th}}$ numerical and analytic solutions in the $j^{\mathrm{th}}$ element of the $k^{\mathrm{th}}$ mesh, respectively. The weights $w_j$ are specified by the type of error calculation. The global error of all solution variables in the device simulation is calculated as

$$\varepsilon_k=\sqrt{\sum_{i}\varepsilon_{ik}^2}. \tag{60}$$

The order of convergence of the FKT equations is determined by the relation

$$|\varepsilon_k|<CN_k^{-p_k}, \tag{61}$$

where $N_k$ is the number of DOF in the mesh, $p_k$ is the approximate order of convergence, and $C$ is a constant.

Two numerical examples are presented to provide insight into the convergence of the discrete FKT equations. The first is a static simulation of the GaN MESFET illustrated in Figure 12. After a quiescent bias of $V_{GS}=-0.5\,V$ and $V_{DS}=4\,V$ is calculated with the static FKT device solver, the global solution variables are saved on a series of meshes. The first and last meshes are the most coarse and dense, respectively. Solutions on the dense mesh are used as the "analytic solutions", $u_{ij,k}$, in Eqn. (59). Figure 13 reports an example of the MESFET mesh refinement strategy used for the following order analysis.

Calculating the global solution variable error, $\varepsilon_k$, requires interpolation of the nodal solution variables on the dense mesh to the nodes of the series of meshes. To this end, linear interpolation is used for its simplicity and efficiency in the post-processing. After the dense mesh solution variables are interpolated to the series of meshes, the global solution variable error is calculated with numerical quadrature. Therefore, the weights $w_j$ in Eqn. (59) represent the volumes of the quadrature simplices.

In Figure 14, the integrated solution variable errors, $\varepsilon_k$, are presented for several series of MESFET mesh refinements. Table 2 reports the integrated errors calculated on each mesh of a single refinement series. The

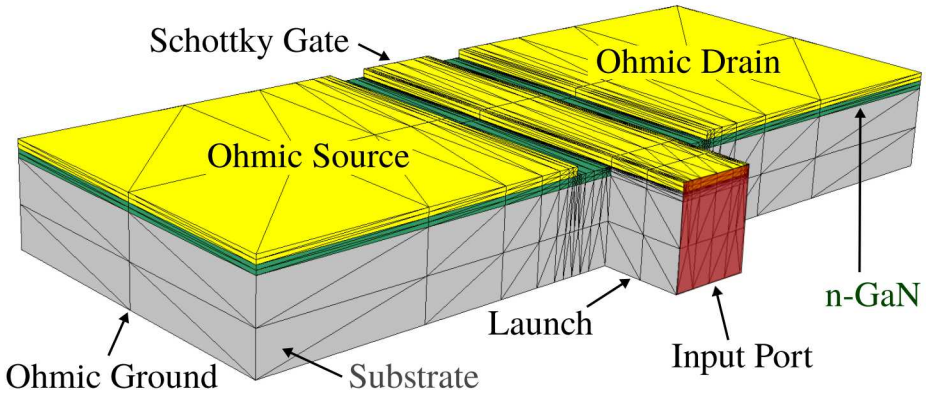


**Fig. 12** An example of the 3D GaN MESFET used to quantify mesh convergence of the FKT device simulation framework. The yellow regions at the top of the mesh are the Ohmic source and drain and the Schottky gate contacts. The bottom surface of the mesh is the Ohmic ground contact (not shown). Total device length is $10\mu$m with a $1\mu$m gate length and a $4\mu$m length of each Ohmic contact. The width of the active device is $4\mu$m. The GaN channel is the dark green region and the insulating substrate is the gray region. The volume labeled "launch" represents the insulating region connected to the voltage port (the red surface).

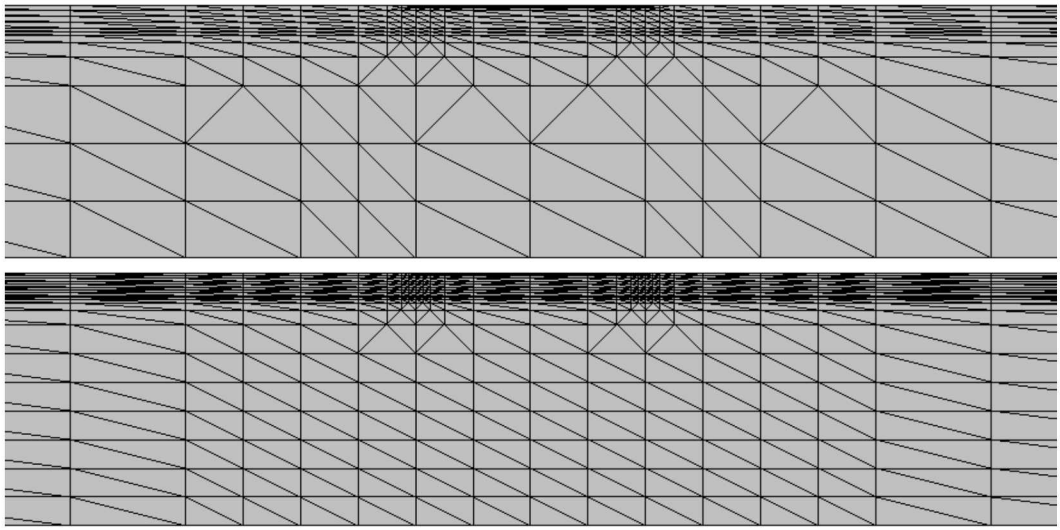

**Fig. 13** An example of mesh refinement of the 3D GaN MESFET example used to quantify the order of convergence of the FKT device simulation equations. The primary mesh is refined by splitting the tetrahedra and the channel under the Schottky gate contact is further refined.

first column lists the DOF corresponding to each mesh. The second and third columns list the solution variable errors, $\varepsilon_k$, and the approximate order of convergence, $p_k$, for each mesh in the series. According to these results, the FKT device simulator exhibits approximately first-order convergence, i.e., $p_k = 1$. This is due to the SG discretization of the particle fluxes [24]. The crux of the SG discretization technique is the approximation of the particle flux vector projections as spatially constant across the primary edges of the DV mesh. This approximation implies first-order mesh convergence.

A pragmatic example of FKT device simulation convergence is an investigation of the static I-V family of a GaN HEMT computed on a series of meshes. This HEMT has previously been investigated in the literature with MC simulations [50], [51] and FKT simula-

| $N_k$ | $\varepsilon_k$ | $p_k$ |
|---|---|---|
| 1041 | 0.12896775 | 3.00 |
| 1646 | 0.03903999 | 2.22 |
| 3034 | 0.01340268 | 1.38 |
| 6283 | 0.00572172 | 1.28 |

**Table 2** Convergence of the static FKT solution variables in the GaN MESFET example with a gate-source bias of $-0.5\,V$ and drain-source bias of $4\,V$.

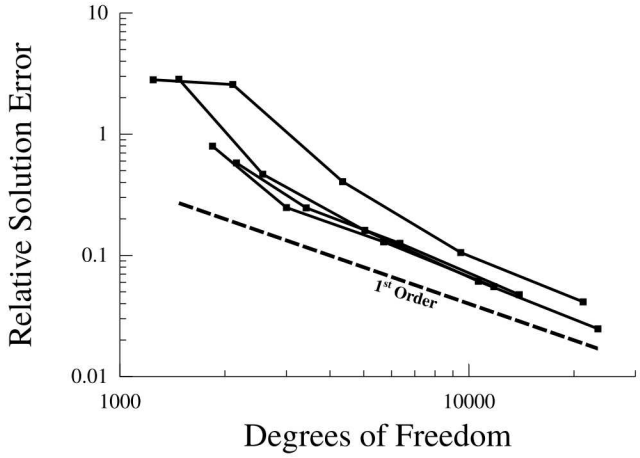


**Fig. 14** Integrated errors, calculated with Eqn. (60), of the 3D GaN MESFET quiescent bias solution variables. Several different series of mesh refinements are presented. An example of the mesh refinement strategy used for the MESFET example is illustrated in Figure 13.

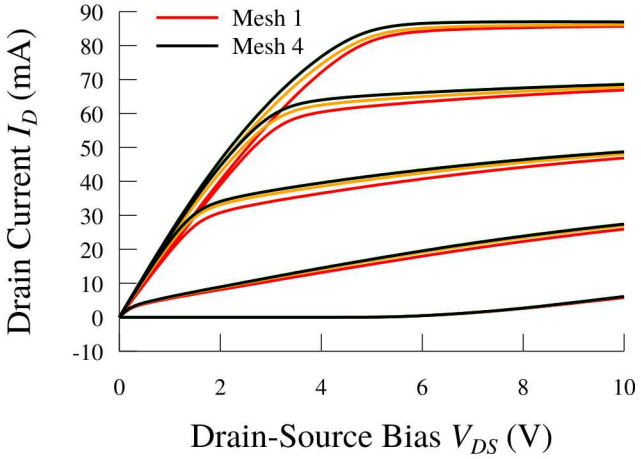


**Fig. 15** The I-V families of the GaN HEMT calculated with the static solver on a series of meshes. The mesh refinement follows a similar strategy to the example of mesh refinement presented in Figure 13.

tions [26], [52]. Device currents are important quantities calculated by the solver. Therefore, it is a useful study to determine how the simulated currents are affected by mesh refinement. The mesh refinement strategy of the HEMT example is similar to the example presented in Figure 13. The error calculation of this example requires evaluation of Eqn. (59) at each drain-source bias. The I-V curves on the dense mesh are used as the "analytic" solutions. Table 3 lists the DOF, global errors in the I-V curves, $\varepsilon_k$, and the corresponding change in the errors, $\Delta\varepsilon_k$. Figure 15 presents the I-V curves calculated on the series of meshes. The change in the device's response becomes negligible after the third mesh refinement. Furthermore, only the linear region of the device's I-V family is moderately affected by the mesh refinement. This type of mesh refinement may not be necessary when simulating the RF response at the peak transconductance of the saturated region of the device.

## 6 Stability of the Discrete FKT Equations

Stability of nonlinear differential equations is a deep and rich subject in systems theory and engineering [53].

| $N_k$ | $\varepsilon_k$ | $\Delta\varepsilon_k$ |
|---|---|---|
| 2277 | 0.05570511 | |
| 2893 | 0.02115591 | -0.03454920 |
| 4513 | 0.00024652 | -0.02090938 |
| 5535 | 0.00002885 | -0.00021767 |

**Table 3** Convergence of the I-V family of the GaN HEMT example calculated with the static FKT solver.

One part of stability theory is the analysis of system equilibria. The analysis starts with a given equilibrium point of the autonomous system $\frac{dx_i(t)}{dt} = F_i(x_i(t))$, i.e., $F_i = 0$. The system of nonlinear differential equations are said to be stable if for a given perturbation of the equilibrium, the solutions return to the equilibrium point [53].

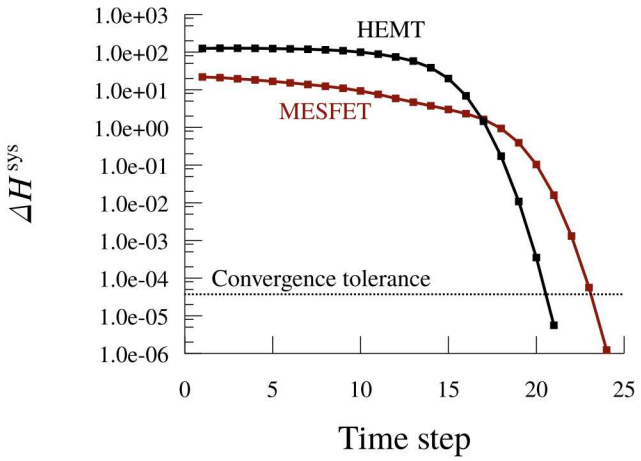


**Fig. 16** Deviation of the numerical enthalpy, Eqn. (63), for the GaN MESFET (red line) and HEMT (black line) examples. Both equilibria are perturbed by displacing two randomly chosen electron gases from their thermal equilibrium states.

The following examples analyze the stability of the discrete FKT equations. The equilibrium points are the solutions of the static solver at thermal equilibrium, i.e., no external biases. After the thermal equilibrium of the specific device example is computed, the total

numerical enthalpy of the system is calculated as

$$H^{\text{sys}} \equiv \sum_i \left[\mathcal{E}_{n,i} + k_B T_i n_i\right] V_i. \tag{62}$$

The superscript "sys" is added to avoid confusion with the magnetic field vector projection, $H_i$, and the discrete heat flux density, $H_{n,ij}$. The enthalpy is calculated from the electron kinetic energy density, $\mathcal{E}_{n,i}$, electron temperature, $k_B T_i$, and electron density, $n_i$, defined in the DUT. The summation represents integration over elements of the DV mesh. Perturbation of the thermal equilibrium amounts to displacing the FKT solutions from their thermal equilibrium states. Two electron gases are randomly chosen and their relative Fermi levels and temperatures are perturbed. The perturbed solutions are used as initial conditions to the quasi-static solver. A transient simulation with no external biases is solved until the discrete residuals reach the global numerical tolerance of the nonlinear solver. The deviation of the total numerical enthalpy is quantified as

$$\Delta H^{\text{sys}} = \left| H^{\text{sys}} - H^{\text{sys}}_{\text{equilib.}} \right|, \tag{63}$$

where $H^{\text{sys}}$ is calculated with Eqn. (62) at each time step of the quasi-static solver and $H^{\text{sys}}_{\text{equilib.}}$ is the numerical enthalpy of the thermal equilibrium solutions, i.e., Eqn. (62) calculated at $t = 0$ before the perturbation. This analysis follows a similar approach to a stability analysis of semiconductor device simulation equations in the literature [54]. The choice of the enthalpy function differs, however. The enthalpy function of this work is chosen for convenience.

Two 3D GaN device examples, the MESFET and the HEMT, are chosen to numerically demonstrate the stability of the discrete FKT equations. For both simulations, two electron gases are randomly chosen and perturbed from their thermal equilibrium states. Figure 16 presents the enthalpy deviation, $\Delta H^{\text{sys}}$, for both device examples. The red line represents the enthalpy deviation versus time step for the GaN MESFET example and the black line presents the same for the GaN HEMT example. An approximate convergence line is illustrated in the figure. Figure 17 presents five more enthalpy deviation simulations of the MESFET example. Each simulation displaced three randomly selected electron gases from their equilibrium states. No perturbation simulation is found to be unstable. Furthermore, each enthalpy deviation approaches an exponential rate of decay near the convergence tolerance. This provides insight into the stability and robustness of the FKT device simulation equations.

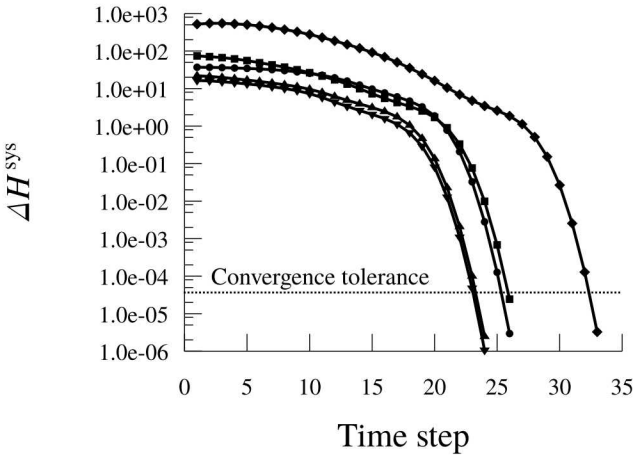


**Fig. 17** Five independent stability analyses of the GaN MESFET example. Each simulation displaced three random electron gases from their equilibrium states. No perturbation is found to be unstable. The enthalpy deviation decays exponentially near the convergence tolerance.

## 7 Conclusion

The FKT device simulator with DVSI discretization can couple nonlinear hot electron transport with full wave EM. The simulation framework can also incorporate electronic band structure, self heating, scattering, and trapping effects. Simulation results suggest that it may provide accuracy comparable to Monte Carlo methods but at a fraction of the computational cost. This accuracy and efficiency could provide a promising simulation alternative for RF device engineering and analysis.

Hot electron and propagating EM wave dynamics are solved simultaneously by exploiting the mutually perpendicular relationship between a Delaunay primary mesh and its Voronoi dual. This relationship was presented in detail along with some additional mesh properties required for high frequency electronic device simulation. For example, the circumcenter of a primary simplex should not lie outside of the simplex's material or outside the problem domain. The planar nature of microelectronics also requires mesh elements with large aspect ratios to represent fluctuations in solution variables while keeping the simulation numerically tractable.

The device equations solved by the simulator were also presented in great detail, both in continuous and in discrete forms, along with necessary boundary conditions and the full-Newton algorithm used to solve the coupled equations. Detailing the specifics in this way may enable independent verification of the simulation methods and results.

The numerical behavior of the discretized device equations were assessed by recording variations in simulation results and convergence characteristics with mesh refinement. This analysis revealed approximately first-order convergence of the nonlinear system. Further tests tracked the evolution of numerical enthalpy as random perturbations in the simulation's variables caused it to follow various trajectories through solution space. These numerical experiments revealed that the simulator's representations of particle and energy dynamics, particularly the entropy maximizing treatment of electronic heat flow through the thermodynamic identity, provide a high degree of stability and robustness. This stability and the numerical efficiency of the FKT/DVSI methodology combined with its fully coupled treatment of both hot electron and propagating EM wave effects may prove useful for computer aided RF device design.

**Acknowledgements** This material is based upon work supported by the Air Force Office of Scientific Research under award number FA9550-17RYCOR495 and the AF STTR program (# FA8650-16-C-1764). Sandia National Laboratories is a multimission laboratory managed and operated by National Technology and Engineering Solutions of Sandia LLC, a wholly owned subsidiary of Honeywell International Inc., for the U.S. Department of Energy's National Nuclear Security Administration under contract DE-NA0003525. This paper describes objective technical results and analysis. Any subjective views or opinions that might be expressed in the paper do not necessarily represent the views of the U.S. Department of Energy or the United States Government.

## References

1. K. Hess, *Advanced Theory of Semiconductor Devices* (Prentice-Hall, Englewood Cliffs, NJ, 2000)
2. C. Jacoboni, *Theory of Electron Transport in Semiconductors: A Pathway from Elementary Physics to Nonequilibrium Green Functions* (Springer Science & Business Media, 2010)
3. N. Metropolis, S. Ulam, Journal of the American Statistical Association **44**(247), 335 (1949)
4. M. Fischetti, S. Laux, Physical Review B **38**(14), 9721 (1988)
5. M. Saraniti, S.M. Goodnick, IEEE Transactions on Electron Devices **47**(10), 1909 (2000)
6. K.J. Willis, S.C. Hagness, I. Knezevic, Journal of Applied Physics **110**, 1 (2011)
7. S. Yamakawa, S. Goodnick, S. Aboud, M. Saraniti, Journal of Computational Electronics **3**(3-4), 299 (2004)
8. T. Sadi, R.W. Kelsall, N.J. Pilgrim, IEEE Transactions on Electron Devices **53**(12), 2892 (2006)
9. S. Russo, A.D. Carlo, IEEE Transactions on Electron Devices **54**(5), 1071 (2007)
10. S. Sridharan, A. Venkatachalam, P.D. Yoder, Journal of Computational Electronics **7**(3), 236 (2008)
11. A. Ashok, D. Vasileska, O.L. Hartin, S.M. Goodnick, IEEE Transactions on Electron Devices **57**(3), 562 (2010)
12. D. Guerra, GaN HEMT modeling and design for millimeter and sub-millimeter wave power amplifiers through Monte Carlo particle-based device simulations. Ph.D. thesis (2011)
13. A.D. Latorre-Rey, F.F.M. Sabatti, J.D. Albrecht, M. Saraniti, Applied Physics Letters **013506**, 111 (2017). DOI 10.1063/1.4991665
14. D.L. Scharfetter, H.K. Gummel, IEEE Transactions on Electron Devices **ED-16**(1), 64 (1969)
15. R. Stratton, Physical Review **126**(6), 2002 (1962)
16. K. Blotekjaer, IEEE Transactions on Electron Devices **ED-17**(1), 38 (1970)
17. T. Grasser, T.W. Tang, H. Kosina, S. Selberherr, Proceedings of the IEEE **91**(2), 251 (2003)
18. Synopsys. Sentaurus device user guide (2013)
19. A. Brannick, N.A. Zakhleniuk, B.K. Ridley, L.F. Eastman, J.R. Shealy, W.J. Schaff, Microelectronics Journal **40**(3), 410 (2009)
20. X.D. Wang, W.D. Hu, X.S. Chen, W. Lu, IEEE Transactions on Electron Devices **59**(5), 1393 (2012)
21. S. Vitanov, V. Palankovski, S. Maroldt, R. Quay, S. Murad, T. Rödle, S. Selberherr, IEEE Transactions on Electron Devices **59**(3), 685 (2012)
22. S. Bhardwaj, B. Sensale-Rodriguez, H.G. Xing, J.L. Volakis, in *2015 73rd Annual Device Research Conference (DRC)* (2015)
23. M. Grupen, Journal of Applied Physics **106**(12), 123702 (2009)
24. M. Grupen, Journal of Computational Electronics **10**(3), 271 (2011)
25. M. Grupen, IEEE Trans. Microwave Theory and Tech. **62**(12), 2868 (2014)
26. M. Grupen, IEEE Transactions on Electron Devices **63**(8), 3096 (2016)
27. A. Franz, G. Franz, S. Selberherr, C. Ringhofer, P. Markowich, IEEE Transactions on Electron Devices **30**(9), 1070 (1983)
28. F. Aurenhammer, R. Klein, D.T. Lee, *Voronoi Diagrams and Delaunay Triangulations* (World Scientific Publishing Co Inc, Singapore, 2013)
29. A. Bowyer, The Computer Journal **24**(2), 162 (1981)
30. D.F. Watson, The Computer Journal **24**(2), 167 (1981)
31. F. Aurenhammer, ACM Computing Surveys (CSUR) **23**(3), 345 (1991)
32. D.T. Lee, B.J. Schachter, International Journal of Computer & Information Sciences **9**(3), 219 (1980)
33. L.P. Chew, in *Proceedings of the third annual symposium on Computational geometry - SCG '87* (ACM Press, New York, New York, USA, 1987), pp. 215–222
34. C. Geuzaine, J.F. Remacle, International Journal for Numerical Methods in Engineering **79**(11), 1309 (2009)
35. H. Si, ACM Transactions on Mathematical Software **41**(2), 1 (2015)
36. Q. Du, V. Faber, M. Gunzburger, SIAM Review **41**(4), 637 (1999)
37. Z.Q. Xie, O. Hassan, K. Morgan, Int. J. Numer. Meth. Engng **87**(July 2010), 48 (2011)
38. I. Sazonov, D. Wang, O. Hassan, K. Morgan, N. Weatherill, Computer Methods in Applied Mechanics and Engineering **195**(13-16), 1826 (2006)
39. S. Walton, O. Hassan, K. Morgan, Computers & Structures **181**, 70 (2017)
40. N. Hitschfeld, P. Conti, W. Fichtner, IEEE Transactions on Computer-Aided Design of Integrated Circuits and Systems **12**(11), 1714 (1993)
41. P. Conti, N. Hitschfeld, W. Fichtner, IEEE Transactions on Computer-Aided Design of Integrated Circuits and Systems **10**(10), 1231 (1991)

42. P. Conti, M. Tomizawa, A. Yoshii, International Journal for Numerical Methods in Engineering **37**(19), 3211 (1994). DOI 10.1002/nme.1620371902
43. Synopsys. Mesh Generation Tools User Guide (2013)
44. J. Krause, On boundary conforming anisotropic Delaunay meshes. Ph.D. thesis (2001)
45. N. Hitschfeld, L. Villablanca, J. Krause, M.C. Rivara, International Journal for Numerical Methods in Engineering **58**(2), 333 (2003)
46. N.C. Miller, J.D. Albrecht, M. Grupen, International Journal of Numerical Modelling: Electronic Networks, Devices and Fields **29**(5), 817 (2016)
47. M. Goano, Solid-State Electronics **36**(2), 217 (1993)
48. S. Sridharan, A. Christensen, A. Venkatachalam, S. Graham, P.D. Yoder, IEEE Electron Device Letters **32**(11), 1522 (2011)
49. Keysight. www.keysight.com (2017)
50. F.A. Marino, N. Faralli, T. Palacios, D.K. Ferry, S.M. Goodnick, M. Saraniti, IEEE Trans. Electron Devices **57**(1), 353 (2010)
51. S.M. Goodnick, M. Saraniti, IEEE Microwave Magazine **13**(7), 36 (2012)
52. N.C. Miller, J.D. Albrecht, M. Grupen, in *2016 74th Annual Device Research Conference (DRC)* (IEEE, 2016), pp. 1–2
53. H.K. Khalil, *Nonlinear systems*, 3rd edn. (Prentice Hall, Upper Saddle River, 2002)
54. A. Jungel, Mathematical Models and Methods in Applied Sciences **5**(4), 497 (1995)